# High Current Density Diamond Photoconductive Semiconductor Switches with a Buried, Metallic Conductive Channel

Zhuoran Han, *Graduate Student Member, IEEE*, Jaekwon Lee, *Graduate Student Member, IEEE*, Stephen Messing, *Graduate Student Member, IEEE*, Thomas Reboli, Andrey Mironov, and Can Bayram, *Senior Member, IEEE*

***Abstract*—Laterally configured diamond photoconductive semiconductor switches (PCSS) with a buried, metallic $p^+$ current channel are reported. Above bandgap ($\lambda \leq 226$ nm) optical triggering enables responsivity of over 130 mA/W. The use of low-impurity semi-insulating diamond as an active absorption layer enables fast rise and fall times (~2 ns) and on/off ratios greater than $10^{11}$. The PCSS excited with a laser energy of 20 nJ per pulse passes a high current density (44 A/cm) under a DC bias of 60 V, thanks to the buried metallic $p^+$ current channel. The reported devices promise high current carrying capacity without the need for filamenting while leveraging the excellent optical, electronic, and thermal properties of diamond.**

***Index Terms*— Diamond, photoconducting devices, power electronics, light triggered switches**

## I. Introduction

PHOCONDUCTIVE semiconductor switches (PCSS) promise high switching frequencies, short rise and fall times, optical triggering, compact footprint, and ultra-high-voltage packaging, making them attractive for high-power switching as well as pulsed high-power technology [1]–[3]. However, conventional PCSS have yet to reach necessary voltage/current levels at the voltage/current slew-rates as required for power grid protection against planned or unplanned grid outages [4]. The use of conventional semiconductors (e.g., Silicon or GaAs) with low critical E-field results in elevated OFF-state power loss and low blocking voltages [5]. In the case of direct-bandgap semiconductors such as GaAs and GaN, high current is enabled in high-gain mode, where one photon generates multiple electron-hole pairs and the current flows through filaments (i.e. high current density paths) rather than uniformly throughout the bulk material [6], [7]. The filamenting, commonly attributed to the impact ionization assisted by photon recycling [8], emits bandgap radiation and is damaging to the PCSS, resulting in short life spans.

Diamond's extraordinary physical properties make it an excellent PCSS semiconductor material that is inherently advantageous for high voltage and high-power switching applications, with practically no limit on thermal resistance. As an ultrawide bandgap (UWBG) semiconductor, diamond has a bandgap of 5.47 eV. Intrinsic diamond has high critical E-field, $E_{critical}$, (10 – 20 MV/cm), high carrier mobility, μ, (up to 2100 $cm^2 \cdot V^{-1} \cdot s^{-1}$ for holes and 1060 $cm^2 \cdot V^{-1} \cdot s^{-1}$ for electrons), and high thermal conductivity, κ, (22 - 24 $W \cdot cm^{-1} \cdot K^{-1}$) [9]. Diamond PCSS, both intrinsic [10] and extrinsic [11], have been investigated utilizing excitation wavelengths above and below the diamond bandgap, respectively. However, these devices have low current density operating in linear mode (e.g., < 0.2 A/cm in [12]). In this study, we demonstrate high current densities in laterally configured diamond PCSS with a buried, metallic conductive channel achieved without the need for carrier multiplication and filamenting. By operating in linear mode (i.e., uniform current conduction without carrier multiplication), the diamond PCSS exhibit fast recovery times and are expected to have better reliability than high-gain mode PCSS.

## II. Experimental

Fig. 1(a) shows the fabrication process of the diamond PCSS, which were based on a 500 μm thick, 4 × 4 $mm^2$ Type IIa high-pressure, high-temperature (HPHT) diamond substrate. A 500 nm thick layer of heavily boron-doped $p^+$ diamond with atomic doping concentration of $5 \times 10^{20}$ $cm^{-3}$ followed by a 1.5 μm thick layer of unintentionally doped layer with atomic boron concentration of $5 \times 10^{15}$ $cm^{-3}$ were grown using microwave plasma enhanced chemical vapor deposition (MPCVD), as in our earlier work [13]. The $p^+$ diamond layer serves as the buried, metallic conductive channel between electrodes. Rectangular metal contacts composed of Ti/Pt/Au were deposited by e-beam evaporation, followed by thermal annealing at 450 ℃ under Ar atmosphere for 1 hour. The metal contacts are Schottky without photoexcitation due to the low active doping concentration in the unintentionally doped layer. However, under illumination the contacts become ohmic due to photogenerated carriers [12]. After cleanroom fabrication, the sample was wire-bonded to a chipset before being connected to the electrical setup.

Fig. 1(b) shows the optical setup used to measure the PCSS performance. Photoconductive measurements were carried out using a tunable optical parametric oscillator (OPO). The OPO laser pulse has a FWHM of 4 ns, a repetition rate of 10 Hz, and a spectral width of approximately 0.1 nm from 230 nm to 210 nm. The laser spot size was fixed to a diameter of 1.75 mm using an iris to keep the laser power density uniform. The total energy incident on the PCSS was controlled using a half-wave

plate (λ/2) and a polarizing beam splitter (PBS). One of the separated beams was blocked, while the other is directed toward the vertically mounted PCSS devices. The laser pulse energy measurement was taken by inserting an energy meter into the beam path of the unblocked beam.

Fig. 1(c) shows the test circuit used to characterize PCSS performance. The test circuit consists of a DC power supply connected in series with diamond PCSS and a Tektronix DPO 7254C oscilloscope with 50 Ω input impedance. The oscilloscope was triggered by a silicon photodiode that detects light scattered from the laser. The OFF-state resistances of PCSS were obtained from current-voltage data using a Keysight B1501A power device analyzer and an EPS 150 TESLA probe station.

## III. Results and Discussion

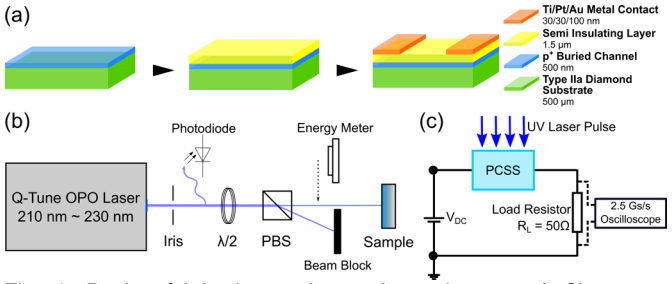


Fig. 1. Device fabrication and experimental setup a) Cleanroom fabrication process of PCSS devices. (b) The optical setup used to measure the PCSS device performance. (c) The electrical setup used for the measurement.

Fig. 2(a) and Fig. 2(b) show the top-view image of the packaged sample and a microscope image of a wire bonded PCSS structure. Three lateral PCSS structures with electrode spacings of 8 μm, 50 μm, and 100 μm were fabricated, and are denoted as PCSS A, B, and C, respectively. All three PCSS devices have the same contact width of 150 μm and contact areas of 0.03 $mm^2$ and 0.14 $mm^2$ for two electrodes. To characterize the response time of the PCSS, the carrier lifetime was estimated by curve fitting the envelope of the temporal response.

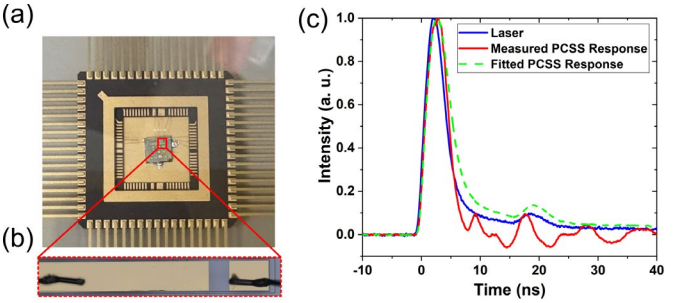


Fig. 2. Diamond buried channel intrinsic PCSS a) Top-view image of the packaged sample. b) Microscope image of a wire bonded PCSS structure. c) A PCSS transient response. Blue curve: transient profile of laser pulse; red curve: transient response of a diamond PCSS; green dashed curve: fitted PCSS response to the envelope of the measured response.

Fig. 2(c) shows a typical transient response measured by the oscilloscope, the exciting laser pulse measured via triggering photodiode, and a fitted PCSS response assuming carrier lifetime $\tau = 0.5$ ns. All three PCSS tested exhibit rise/fall times (10 - 90 %) of about 2 ns, which is limited by the rise/fall time of the laser pulse and promises extremely high slew rate if scaled to higher voltages.

Fig. 3(a) shows the measured peak photocurrent density of PCSS C in the spectral range of 210 nm to 230 nm, with a fixed incident optical energy of 30 μJ/pulse and a constant DC bias voltage of 40 V. Peak photocurrent density increased significantly from 1.08 A/cm to 6.28 A/cm as the laser wavelength decreased from 226 nm to 222 nm. This change in peak photocurrent corresponds to the sharp increase in the measured absorption coefficient above diamond's bandgap $E_G = 5.47$ eV, which increases from $24.04 \pm 2.67$ $cm^{-1}$ at the wavelength of 226 nm to $245.60 \pm 27.31$ $cm^{-1}$ at 222 nm. The much-improved responsivity at shorter wavelengths implies that above-bandgap excitations are advantageous for achieving high efficiencies in lateral diamond PCSS.

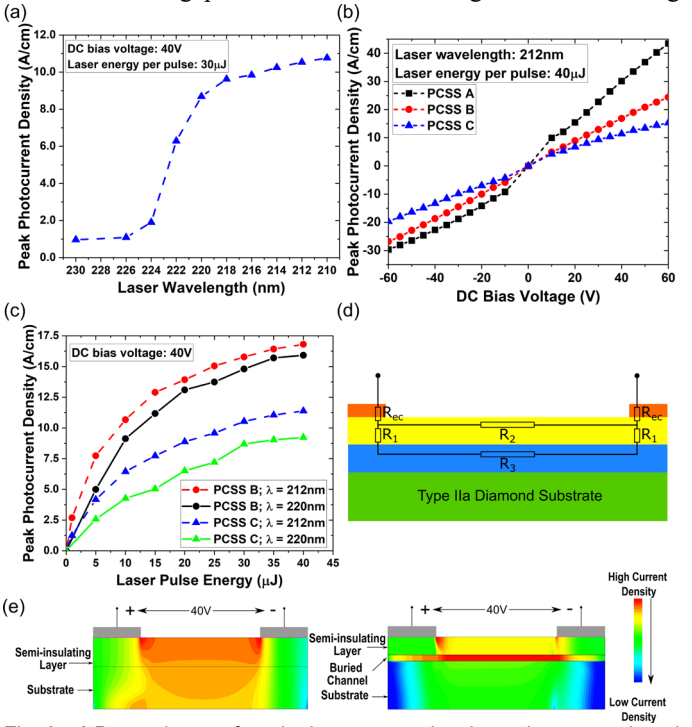


Fig. 3. a) Dependence of peak photocurrent density on laser wavelength for a PCSS device. (b) Dependence of peak photocurrent density on the DC bias voltage for three PCSS devices. (c) Dependence of peak photocurrent density on laser pulse energy. (d) Equivalent circuit model of buried channel PCSS. (e) Simulated current density distribution in logarithmic scale inside (left) a conventional PCSS and (right) a buried channel PCSS.

The photo response of the PCSS devices were characterized under DC bias voltages between -60 V to 60 V. Fig. 3(b) shows the dependence of peak photocurrent density on the DC bias voltage for three PCSS devices. The laser wavelength is fixed at 212 nm, which corresponds to a photon energy above the diamond bandgap, and the incident optical energy is fixed to 40 μJ/pulse, which corresponds to a peak incident intensity of 415.7 kW/$cm^2$. The effective energy incident on each PCSS is 20.0 nJ, 124.6 nJ, and 249.5 nJ per laser pulse for PCSS A, B, and C, respectively. The linear peak photocurrent density $J$ is calculated by dividing the peak current through the 50 Ω input resistor with the width of the contact. PCSS A with 8 μm spacing exhibits the highest current density of 43.5 A/cm at 60 V bias among three devices, corresponding to a responsivity

of 130.3 mA/W. Here, the responsivity is calculated using the laser FWHM of 4 ns and the effective energy per laser pulse. The overall performance of three PCSS devices is summarized in Table 1, where responsivity is normalized with the vertical electric field across the semi-insulating layers.

TABLE I
SWITCH PERFORMANCE OF 3 PCSS DEVICES TESTED

| # | Spacing (μm) | $R_{OFF}$ (GΩ) | $R_{ON}$ (Ω) | $\frac{R_{OFF}}{R_{ON}}$ | Peak $J$ (A/cm) | Responsivity (mA-cm/W-kV) |
|---|---|---|---|---|---|---|
| A | 8 | 0.24 | 72.1 | $3.3\times10^{6}$ | 43.5 | 3.55 |
| B | 50 | $4\times10^{4}$ | 121.5 | $3.3\times10^{11}$ | 24.4 | 0.38 |
| C | 100 | $4\times10^{4}$ | 211.4 | $1.9\times10^{11}$ | 15.3 | 0.15 |

At a DC bias of 60V and excited by 40 μJ, 212 nm laser pulses

Fig. 3(c) shows the peak photocurrent density as a function of incident optical energy. PCSS B and C were tested at a constant DC bias voltage of 40 V and two laser wavelengths of 212 nm and 220 nm. At both wavelengths, as optical power increases, the photocurrent starts to saturate due to invariant resistances in contacts and the buried channel.

To visualize the effect of the buried channel, an equivalent circuit model of buried channel PCSS is shown in Fig. 3(d), where the total resistance of the PCSS is expressed as:

$$R_{PCSS} = 2R_{ec} + \{R_2||(2R_1 + R_3)\} \quad (1)$$

Here, $R_1$, $R_2$ are the resistances for the vertical and horizontal current flow in the semi-insulating layer, $R_3$ is the resistance of the buried channel, $R_{ec}$ is the effective contact resistance under illumination, and $R_{PCSS}$ is the minimum PCSS resistance in the ON-state calculated from experimental data by applying the voltage divider rule to the 50 Ω input resistor:

$$R_{PCSS} = \frac{V_{DC}\times 50\Omega}{V_{50\Omega}} - 50\ \Omega \quad (2)$$

where $V_{DC}$ is the power supply DC voltage, and $V_{50\Omega}$ is the peak voltage measured by the oscilloscope. In (1), $R_3$ and $R_{ec}$ are calculated using the saturated photocurrents in Fig. 3(c) assuming $R_2 \gg R_3$: when the optical power increases, $R_1$ becomes negligible but $R_3$ and $R_{ec}$ remain relatively constant. Next, $R_1$ and $R_2$ are estimated by linear fitting the $I$-$V$ curves. Here, it is assumed that $R_2$ and $R_3$ are proportional to the separation of two contacts, and $R_1$ and $R_{ec}$ are the same for all devices under the same photoexcitation condition. The values of $R_1$, $R_2$, $R_3$, and $R_{ec}$ for three PCSS devices are tabulated in Table 2.

TABLE II
CALCULATED EQUIVALENT CIRCUIT MODEL RESISTANCES

| PCSS # | $R_1$ (Ω) | $R_2$ (Ω) | $R_3$(Ω) | $R_{ec}$ (Ω) |
|---|---|---|---|---|
| A | 11 | 111 | 7 | 36 |
| B | 11 | 694 | 41 | 36 |
| C | 11 | 1387 | 82 | 36 |

At a DC bias of 40V and excited by 40 μJ, 212 nm laser pulses

From the equivalent resistance values, it is estimated that in PCSS B, 92% of current conduction is through the buried channel, while in the PCSS C with twice the channel length, 93% of conduction is through the buried channel. Fig. 3(e) shows the current density distribution based on Synopsys Sentaurus TCAD simulation at a DC bias voltage of 40 V and under the illumination of 212 nm light with intensity of 10 kW/cm$^2$ inside a traditional and a buried channel PCSS with electrode spacing of 50 μm, respectively [14]. In lateral PCSS with a buried, metallic conductive channel, current conduction is concentrated inside the heavily doped channel, while in traditional PCSS the current density is evenly distributed inside the semi-insulating layer. The TCAD simulation is consistent with fitted results based on measurement data and implies that the addition of the metallic buried channel greatly reduces the total ON-state resistance of PCSS.

Fig. 4 benchmarked the on/off ratio vs. laser energy of our PCSS against previously reported PCSS devices. By utilizing the semi-insulating diamond layer and above bandgap photoexcitation, we achieve large on/off ratios using a low-energy laser source [6], [12], [15]–[22].

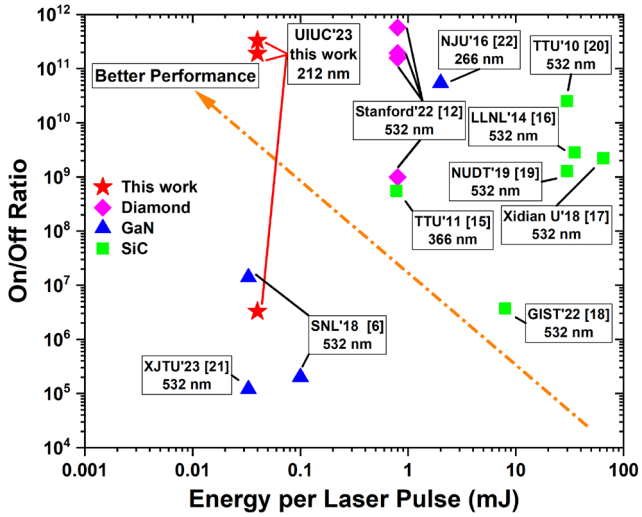


Fig. 4. Benchmark of the tested PCSS devices against prior diamond, GaN, and SiC PCSS in terms of on/off ratio vs. energy per laser pulse. The excitation wavelengths used in each study are shown [6], [12], [15]–[22].

## IV. CONCLUSION

In conclusion, diamond lateral PCSS with a buried, metallic $p^+$ current channel are demonstrated with above bandgap optical triggering. The PCSS devices exhibit large on/off ratios (>$10^{11}$), fast rise/fall times (~2 ns) and high current densities (44 A/cm). The PCSS devices exhibit linear current-voltage characteristics up to DC bias of +/- 60 V, implying that even higher current densities are possible before carrier velocity saturation occurs. TCAD simulation and experimental data predicts that over 90% of current conduction is through the buried, metallic conductive channel. The buried channel design enables higher photocurrents during the ON-state utilizing the high conductivity $p^+$ channel, while still maintaining large OFF-state resistances. This study's results advocate new designs for PCSS to realize higher ON-state current and efficiency.

## REFERENCES

[1] S. Doğan *et al.*, "4H–SiC photoconductive switching devices for use in high-power applications," *Appl Phys Lett*, vol. 82, no. 18, pp. 3107–3109, May 2003, doi: 10.1063/1.1571667.

[2] J. H. Leach, R. Metzger, E. A. Preble, and K. R. Evans, "High voltage bulk GaN-based photoconductive switches for pulsed power applications," J.-I. Chyi, Y. Nanishi, H. Morkoç, J.

Piprek, E. Yoon, and H. Fujioka, Eds., Mar. 2013, p. 86251Z. doi: 10.1117/12.2005548.

[3] F. J. Zutavern *et al.*, "Photoconductive semiconductor switch experiments for pulsed power applications," *IEEE Trans Electron Devices*, vol. 37, no. 12, pp. 2472–2477, Dec. 1990, doi: 10.1109/16.64520.

[4] E. Majda-Zdancewicz, M. Suproniuk, M. Pawłowski, and M. Wierzbowski, "Current state of photoconductive semiconductor switch engineering," *Opto-Electronics Review*, vol. 26, no. 2, pp. 92–102, May 2018, doi: 10.1016/j.opelre.2018.02.003.

[5] G. M. Loubriel *et al.*, "Photoconductive semiconductor switches," *IEEE Transactions on Plasma Science*, vol. 25, no. 2, pp. 124–130, Apr. 1997, doi: 10.1109/27.602482.

[6] E. A. Hirsch *et al.*, "High-Gain Persistent Nonlinear Conductivity in High-Voltage Gallium Nitride Photoconductive Switches," in *2018 IEEE International Power Modulator and High Voltage Conference (IPMHVC)*, IEEE, Jun. 2018, pp. 45–50. doi: 10.1109/IPMHVC.2018.8936660.

[7] W. Shi *et al.*, "30 kV and 3kA semi-insulating GaAs photoconductive semiconductor switch," *Appl Phys Lett*, vol. 92, no. 4, Jan. 2008, doi: 10.1063/1.2838743.

[8] A. R. Chowdhury, J. C. Dickens, A. A. Neuber, R. Ness, and R. P. Joshi, "Lock-on physics in semi-insulating GaAs: Combination of trap-to-band impact ionization, moving electric fields and photon recycling," *J Appl Phys*, vol. 123, no. 8, Feb. 2018, doi: 10.1063/1.5013248.

[9] N. Donato, N. Rouger, J. Pernot, G. Longobardi, and F. Udrea, "Diamond power devices: State of the art, modelling, figures of merit and future perspective," *Journal of Physics D: Applied Physics*, vol. 53, no. 9. Institute of Physics Publishing, 2020. doi: 10.1088/1361-6463/ab4eab.

[10] P. K. Bharadwaj, R. F. Code, H. M. van Driel, and E. Walentynowicz, "High voltage optoelectronic switching in diamond," *Appl Phys Lett*, vol. 43, no. 2, pp. 207–209, Jul. 1983, doi: 10.1063/1.94288.

[11] D. L. Hall *et al.*, "Photoconductive Switch with High Sub-Bandgap Responsivity in Nitrogen-Doped Diamond," *IEEE Electron Device Letters*, vol. 41, no. 7, pp. 1–1, Jul. 2020, doi: 10.1109/LED.2020.2999821.

[12] K. Woo, M. Malakoutian, B. A. Reeves, and S. Chowdhury, "A study on sub-bandgap photoexcitation in nitrogen- and boron-doped diamond with interdigitated device structure," *Appl Phys Lett*, vol. 120, no. 11, Mar. 2022, doi: 10.1063/5.0083710.

[13] Z. Han and C. Bayram, "Diamond p-Type Lateral Schottky Barrier Diodes With High Breakdown Voltage (4612 V at 0.01 mA/Mm)," *IEEE Electron Device Letters*, vol. 44, no. 10, pp. 1692–1695, Oct. 2023, doi: 10.1109/LED.2023.3310910.

[14] "Version T-2022.03, Synopsys Inc., Mountain View, CA, USA, 2022."

[15] C. James, C. Hettler, and J. Dickens, "Design and Evaluation of a Compact Silicon Carbide Photoconductive Semiconductor Switch," *IEEE Trans Electron Devices*, vol. 58, no. 2, pp. 508–511, Feb. 2011, doi: 10.1109/TED.2010.2089689.

[16] J. S. Sullivan, "High power operation of a nitrogen doped, vanadium compensated, 6H-SiC extrinsic photoconductive switch," *Appl Phys Lett*, vol. 104, no. 17, p. 172106, Apr. 2014, doi: 10.1063/1.4875258.

[17] P. Cao, W. Huang, H. Guo, and Y. Zhang, "Performance of a Vertical 4H-SiC Photoconductive Switch With AZO Transparent Conductive Window and Silver Mirror Reflector," *IEEE Trans Electron Devices*, vol. 65, no. 5, pp. 2047–2051, May 2018, doi: 10.1109/TED.2018.2815634.

[18] P. H. Choi *et al.*, "Output Characteristics of Side-Illuminated Photoconductive Semiconductor Switch Based on High Purity Semi-Insulating 4H-SiC," *IEEE Access*, vol. 10, pp. 109558–109564, 2022, doi: 10.1109/ACCESS.2022.3214654.

[19] Q. Wu, T. Xun, Y. Zhao, H. Yang, and W. Huang, "The Test of a High-Power, Semi-Insulating, Linear-Mode, Vertical 6H-SiC PCSS," *IEEE Trans Electron Devices*, vol. 66, no. 4, pp. 1837–1842, Apr. 2019, doi: 10.1109/TED.2019.2901065.

[20] C. James, C. Hettler, and J. Dickens, "High voltage photoconductive switches using semi-insulating, vanadium doped 6H-SiC," in *2009 IEEE Pulsed Power Conference*, IEEE, Jun. 2009, pp. 283–286. doi: 10.1109/PPC.2009.5386303.

[21] X. Yang *et al.*, "The Initial Test of a Micro-Joules Trigger, Picosecond Response, Vertical GaN PCSS," *IEEE Photonics Technology Letters*, vol. 35, no. 2, pp. 69–72, Jan. 2023, doi: 10.1109/LPT.2022.3222163.

[22] Y. Chen, H. Lu, D. Chen, F. Ren, R. Zhang, and Y. Zheng, "High-voltage photoconductive semiconductor switches fabricated on semi-insulating HVPE GaN:Fe template," *physica status solidi c*, vol. 13, no. 5–6, pp. 374–377, May 2016, doi: 10.1002/pssc.201510210.